Hindawi
Advances in Civil Engineering
Volume 2023, Article ID 6865847, 9 pages
https://doi.org/10.1155/2023/6865847

Research Article

An Experimental Study of GPR Near-Field Problem in Depth Ranging of Buried Objects

Rex Yui Kei Cham and Wallace Wai Lok Lai

The Hong Kong Polytechnic University, Room ZS615, 6/F, Block Z South, Hung Hom, Kowloon, Hong Kong

Correspondence should be addressed to Wallace Wai Lok Lai; wllai@polyu.edu.hk

Received 30 March 2023; Revised 5 August 2023; Accepted 24 August 2023; Published 4 October 2023

Academic Editor: Suraparb Keawsawasvong

We evaluate the often neglected ranging (or cover depth) error of an object located within the Fresnel Region (or called radiating near-field) and reactive near-field region in ground penetrating radar (GPR). The experiments were conducted in concrete specimens with various rebar cover depths from 10 to 80 mm, which imitates any object imaged by GPR from reactive near-field, Fresnel region to far-field region. Velocities of each individual data point of the hyperbolic reflections of the embedded reinforcement in radargram are calculated by developed algorithms based on common offset antenna and multiple trilaterated ray paths. Two different velocity algorithms, based on semi- and full-trilaterated ray paths, were applied to estimate the wave travelling velocity as a prerequisite of cover depth measurement. The algorithms were firstly validated using a high-frequency 2-GHz antenna to verify the travelling speed of radar waves in air, which is equal to the speed of light. Then, the same antenna was used to estimate the cover depth by measuring the time of flight and velocity based on the two velocity algorithms. The results reveal that the ranging accuracy is highly in doubt in reactive near-field and Fresnel regions but is largely improved when the object locates in far-field region where GPR wave propagation becomes plane-type. The measurements, riding on accurate modelling of ray-path's trilateration models, provide evidence that the normal linear scale of GPR time-to-depth conversion overlooks the effects of near-field/Fresnel region. We therefore suggest that the GPR near-field/Fresnel region and far-field boundary must be taken into account before any attempt of time-to-depth conversion and depth estimation of objects by GPR are carried out.

1. Introduction

Ground penetrating radar (GPR) transfers energy via the antenna to substrate surface by quasi-stationary fields, induction fields, and radiated fields. Energy is exchanged in the reactive near field. Target coupled energy from the source fields and signal will be coupled in the antenna in the far-field regions (or called radiated field) [1]. It is crucial to understand the boundary of near-field and far-field region. These two regions relate to the geometric dimensions of the source (D), i.e., the maximum linear dimension of the radiator and the energy emitted by the source dominant wavelength (λ). Region to separate near field and radiating far field is expressed as $r = 2D^2/\lambda$, where r is the distance of the dipole element to the concerned point [1–3]. The near-field region can be further separated into reactive near-field and Fresnel region (or called radiating near field), and the boundary is expressed as $r = 0.62\sqrt{D^3/\lambda}$. This mathematical derivation between antenna dipole design as reflected by (D) and material properties as reflected by λ is, therefore, an important but often neglected factor on a near-surface geophysical and engineering application on GPR: *depth ranging of an object*. For the former, i.e., the mathematical derivation of a physical phenomenon, is clearly a nonlinear problem. But for the latter, i.e., the depth ranging of an object, is usually regarded as a linear problem where depth = two-way travel time × velocity divided by 2. It is clear that the linear solution of the latter is far from adequate to fully represent the nonlinear nature of the former physical phenomenon. This study will illustrate that the oversimplified linear solution is highly constrained in reactive near-field and Fresnel zones but works fairly well in the far-field zone. Yet, the oversimplified linear solution is often applied in two focus areas of GPR, i.e., structural inspections and underground utility surveys.

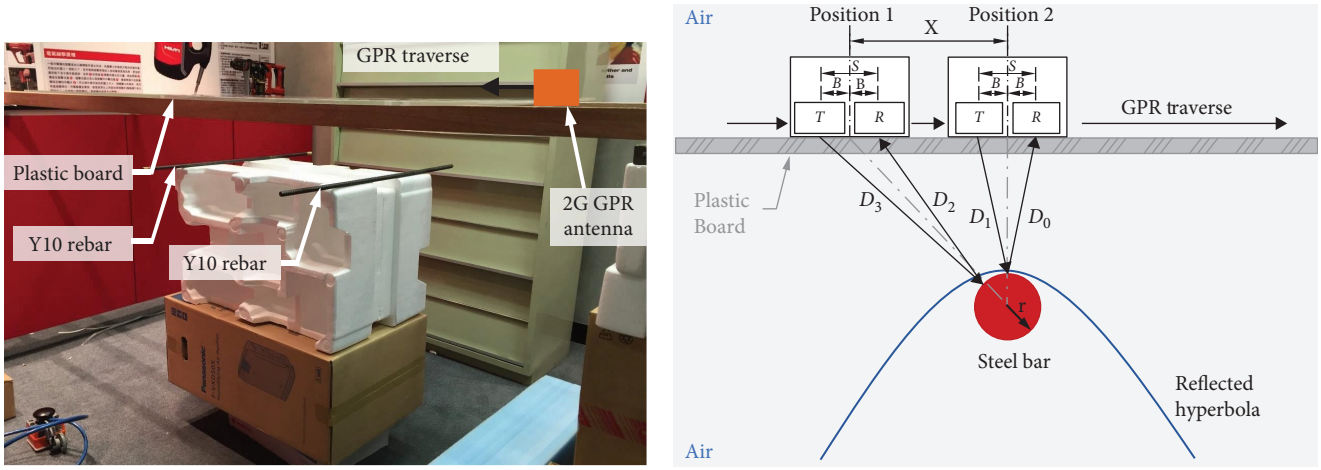

(a) (b)

Figure 1: (a) Photos of the experimental setup and the corresponding and (b) schematic drawing of the calibration process in air.

Structural inspections on the quality of reinforced concrete elements during construction and regular structural health monitoring of existing structures are crucial to guarantee the integrity and serviceability of the structures. During inspection, the measurement of the actual cover depth of reinforcements and tendon ducts is an important criterion of the quality of the structure, which serves two purposes. The first is a compliance check against the design drawings in new works. The second is long-term durability, resisting aggressive agents like carbonation and chloride attack in maintenance and addition and alternation works. Another example is the survey of the cover thickness of underground utilities [4–13]. Unlike concrete, which is a relatively homogeneous environment to host rebar and tendon ducts, underground conditions are much more complex and inhomogeneous to host utilities. Nowadays, the building of 3D as-built data infrastructure on the unknown city underground is prevailing because of the ability of handling huge amounts of data in building information modelling. Building of such data infrastructure requires cover depth as an important attribute, and GPR is one of the two geophysical technologies, while the other is electromagnetic locating. The two focus areas thus justify the requirement of accurate cover depth estimation and the underlying theories of reactive near-field, Fresnel zone, and far-field in the GPR world.

In this study, concrete specimens with various rebar cover depths from 10 to 80 mm were used to imitate any object imaged by GPR from reactive near-field, Fresnel region to far-field region. Concrete is used because of its relatively small size of handling and relatively homogeneous environment compared to soil. Rebar is a perfect reflector in concrete to generate strong signal reflection. A GSSI 2 GHz palm bowtie antenna was used to acquire the smallest geometric dimension of the source (D) and also a small wavelength in concrete ($\sim$50 mm for a velocity of 0.1 m/ns). This experiment can be upscaled to other object dimensions and antenna frequencies by following the discussion in the first paragraph of Section 1. A standard measurement method of cover depth is proposed by comparing two developed velocity algorithms [14, 15] with consideration of full trilaterated ray paths. The method was first validated in a control experiment with air as a homogeneous medium of wave velocity and then applied in reinforced concrete specimens, as described in Section 2.

2. Experimental Setup and Data Collection

2.1. Experimental Setup and Data Collection in Air. The experimental setup included a thin plastic board and two Y10 steel rebars. Rebars were placed on an 860-mm height foam box, and the distance between the GPR antenna and rebar was adjusted to 185 mm, as shown in Figure 1. The 2 GHz antenna was used to scan the Two Y10 steel rebars for data collections. Twelve repetitive radar measurements were done. The radargram obtained was used for velocity analysis and for the verification test. Velocity analytical method using semi-trilateration Equation (3) [14] and combined equations/full-trilateration Equations (1), (3), and (4) [15] were used to measure the velocity of the reflected wave.

2.2. Experimental Setup and Data Collection in Controlled Experiments. Four reinforced concrete beams with dimensions of 200 mm (width) $\times$ 800 mm (long) $\times$ 110 (depth) were cast (Figure 2). Each beam was cast with two diameters, 20-mm rebars with 300-mm constant spacing between each rebar were fixed at 250 mm away from the end of the beam. Two rebars were casted with the same cover depth from the concrete surface. Another three pairs of rebars were cast into three concrete beams, and totally eight different cover depths of rebars from the concrete face from 10 to 80 mm were cast. The only variable of each beam setup was the cover depth of two rebars, where the cover depths for pairs of rebars were the same. Radar measurements were done after the casting of concrete at 120 and 180 days. A 2-GHz high centre frequency antenna provides a high-resolution measurement of time and distance for shallow cover depth reinforcement in radargram, and a shorter wavelength of propagated wave matches the measurement of diameter of reinforcement, i.e., 20-mm diameter. There were 12 scans of each cover depth at different

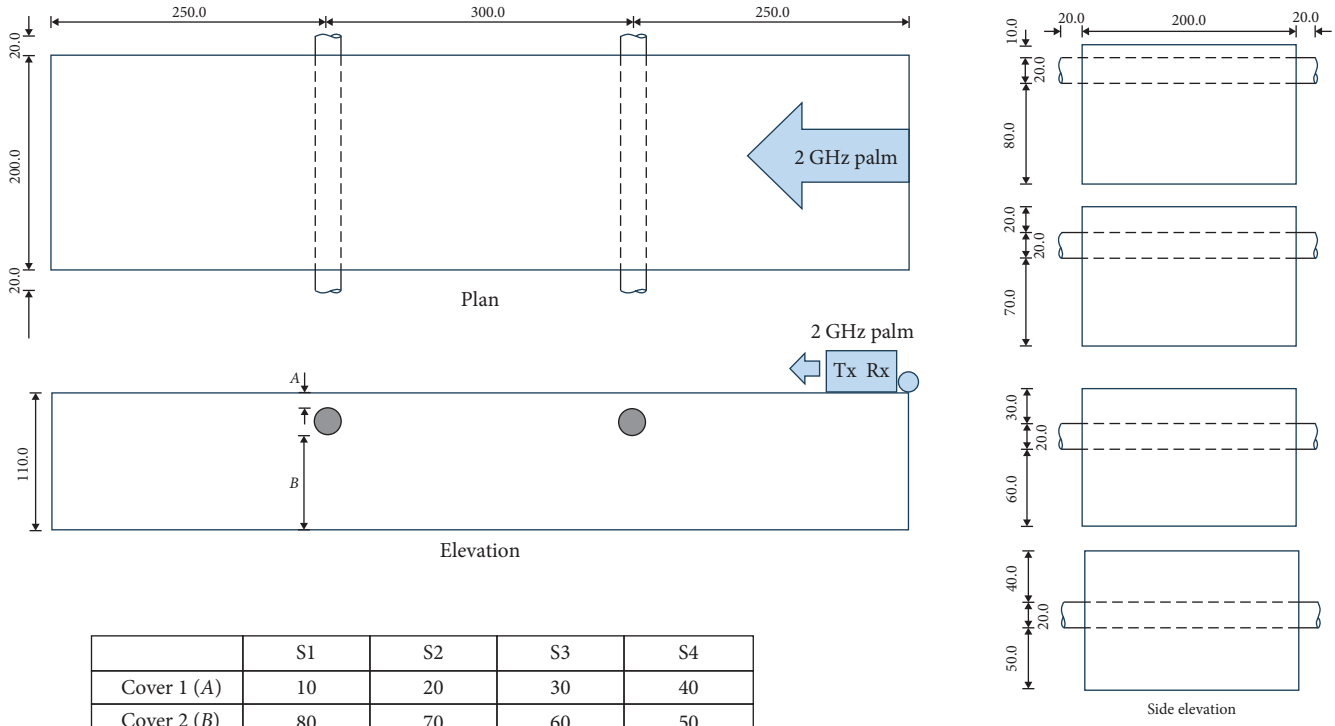

	S1	S2	S3	S4
Cover 1 (A)	10	20	30	40
Cover 2 (B)	80	70	60	50
	S5	S6	S7	S8
Cover 1 (A)	80	70	60	50
Cover 2 (B)	10	20	30	40

Figure 2: The experimental setup of the stimulated beam.

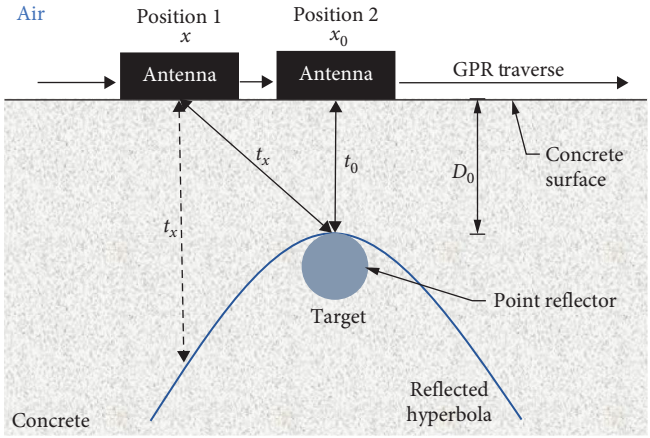

Figure 3: The reflection model for GPR wave propagation and reflection.

days, and a total of 384 scans were processed for 2D signal processing and radargram display by commercial software, i.e., Reflexw. Velocity measurement based on the trilateration models with hyperbolic fitting developed in Sham and Lai [14], as shown in Figure 3, was performed by an in-house programme in LabVIEW. Since the receiver and transmitter are configurated with a common offset distance and shielded in a container, the travelled path of the GPR wave was estimated by Pythagoras theorem.

In the 2D signal processing, the adjustment of waveform using direct current shift and standard dewow, and time zero correction, which reference to the ground, were conducted. The background and equipment gain of the signal were removed. After signal processing, extraction of data from radargram and velocity analysis of the diffractive hyperbolas were performed by the developed algorithms, in an in-house LabVIEW programme. The point of inflection at the direct wave of each reflected A-scan was programmed to form hyperbolas correspondent to the rebar and calculating the velocities [16]. With measured time of flight at the apex of hyperbolas, the cover depth of the rebars can be measured and compared with the actual values.

3. Data Processing

GPR antenna (with ordinary common offset configuration) traverse runs perpendicular to the alignment of rebar, or the parallel orientated GPR dipoles/E-field with the rebar alignment sets in the same direction during scanning. The GPR wave spreads a conical form of footprint (or called first fresnel zone), penetrates downward through a lossless media, and reaches a circular object, i.e., rebar, with significant dielectric contrast with the host material, i.e., concrete.

The reflected signal received will appear as a diffractive hyperbola in the radargram. The wave velocity associated with the corresponding spatial and lateral distance (x) to measured wave travelling time (t) can be determined by the slope of the hyperbola, as seen in Figure 3. The location and depth of rebar from the concrete surface can then be calculated. Therefore, to analyse wave velocity, it is crucial to model the reflected diffractive hyperbola accurately. Velocity estimation for antenna with common offset configuration can be determined by one or more than one of the following combination methods:

(a) Velocity algorithm

The equation estimates the GPR wave velocity by measuring the travelling time to and from the GPR and the object, i.e., two-way travel time, and the depth of the object from a flat surface.

$$v = \frac{2D_0}{t}, \tag{1}$$

where t = measured time for GPR wave to travel in between antenna and the object and D_0 = distance between target object and surface of host material.

(b) Velocity algorithm—method in ASTM D6432—2020 [17] (circular object and single trilaterated method)

The equation is based on the assumption that the target object and GPR antennas, i.e., transmitter and receiver, are point-form sources. Antenna separation distance and objects size are not considered.

$$v(x_i) = \left(\frac{2}{t_0}\right)\left[\frac{x_i}{\sqrt{\left(\frac{t_i}{t_0}\right)^2 - 1}}\right], \tag{2}$$

where x_i = distance between the transmitting antenna at an oblique position "i" and receiving antenna at a position where the apex of hyperbola is located at. It is considered that the traverse of GPR antenna and the alignment of the object are at right angle, t_i = measured time for GPR wave to travel in between antenna and the object where antenna located at position "i," t_0 = measured time for GPR wave to travel in between the antenna and the object where the antenna is located on top of the object, i.e., location of apex of hyperbola.

(c) Velocity algorithm—point form target and measured by trilaterated ray-path method

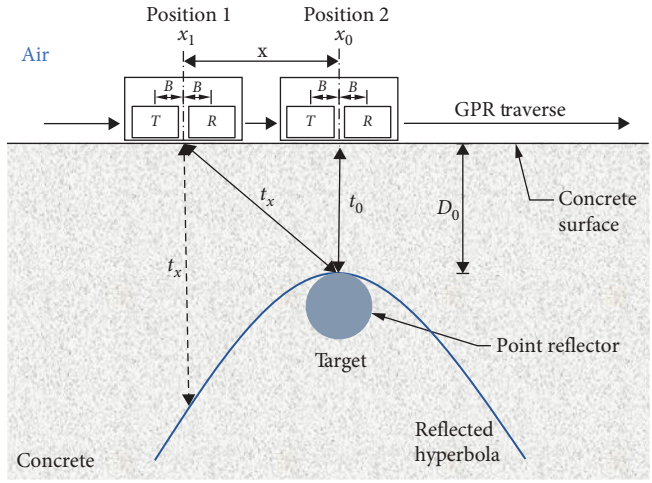

FIGURE 4: The reflection model for GPR wave propagation and reflection with consideration of antenna separation.

The equation considered the separation distance between transmitter and receiver ($2B$) of a monostatic antenna and the oblique angle (θ) between the travel of GPR antenna and the alignment of the object, as shown in Figure 4.

$$v(x_i) = \sqrt{\frac{2(x_i\sin\theta)^2 t_i \pm 2x_i\sin\theta((x_i\sin\theta)^2 t_i^2 - 4B^2 t_i^2 + 4B^2 t_0^2)^{0.5}}{t_i^3 - t_0^2 t_i}}, \tag{3}$$

where x_i = distance between antennas at position "i" and antenna at a position where the apex of hyperbola is located at, θ = angle between the traverse of GPR antenna and the alignment of rebar, B = distance between mid-point of the monostatic antenna and Tx and Rx antennas respectively, t_i = measured time for GPR wave to travel between antenna and the object where antenna located at any oblique position "i," t_0 = measured time for GPR wave to travel in between antenna and the object where antenna located on top of the object, i.e., location of apex of hyperbola.

(d) Velocity algorithm—trilaterated ray path with known parameters/available information, size and depth of target object

The equation incorporated known parameters/available information from an as-built record drawing of the target object into consideration, including the size and depth of the object from the surface of host material [14, 18], as shown in the programming platform in Figures 5 and 6.

$$v(x_i) = \frac{\sqrt{\left[(D_0+r) - \frac{(D_0+r)r}{\sqrt{(D_0+r)^2+(x_i\sin\theta)^2}}\right]^2 + \left[\left(x_i - \frac{r(x_i\sin\theta)}{\sqrt{(D_0+r)^2+(x_i\sin\theta)^2}}\right) - B\right]^2} + \sqrt{\left[(D_0+r) - \frac{(D_0+r)r}{\sqrt{(D_0+r)^2+(x_i\sin\theta)^2}}\right]^2 + \left[\left(x - \frac{r(x_i\sin\theta)}{\sqrt{(D_0+r)^2+(x_i\sin\theta)^2}}\right) + B\right]^2}}{t_{x_i}}, \tag{4}$$

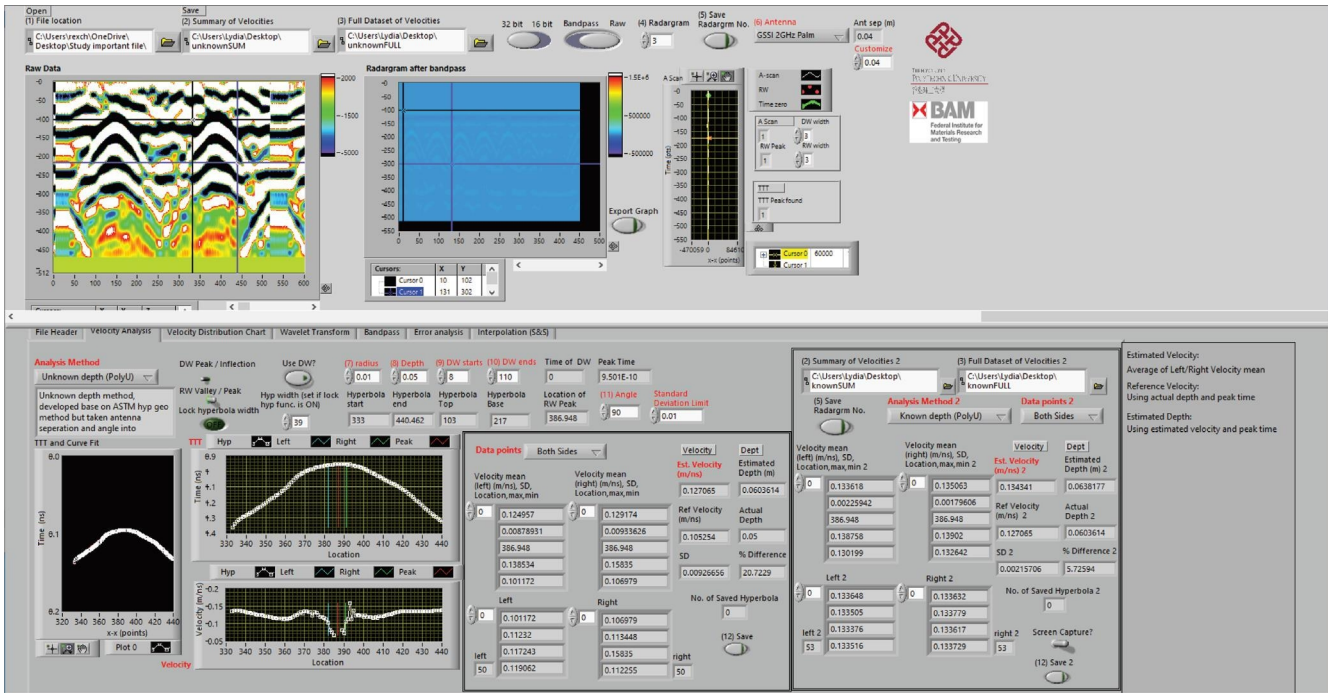

Figure 5: The graphical user interface of the LabVIEW velocity analysis programme.

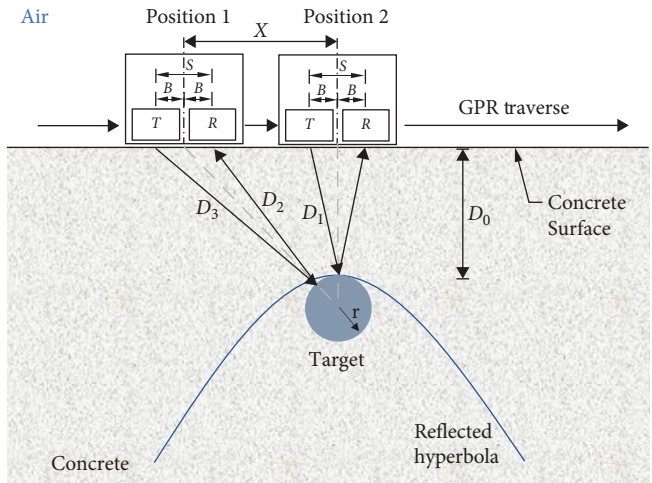

Figure 6: Schematic diagram of the multitrilaterated ray-path geometry of the common-offset survey of shielded antenna.

where x_i = distance between antennas at position "i" and antenna at a position where the apex of hyperbola is located at, θ = angle between the travel of GPR antenna and the alignment of rebar, D_0 = distance between target object and surface of host material based on Equations (1) and (3), r = size of round-shaped object, i.e., radius, B = distance between mid-point of the monostatic antenna and Tx and Rx antennas, respectively, t_{x_i} = measured time for GPR wave to travel in between antenna and the object where antenna located at position "i," t_0 = measured time for GPR wave to travel in between antenna and the object where antenna located on top of the object, i.e., location of apex of hyperbola.

Angle "θ" can be measured from the grid of the GPR antenna traverse and alignment of rebar after obtaining it in 3D simulation. The size of the object "r" and distance of antenna separation can be obtained via an as-built record drawing and manufacturer's specification, respectively. However, distance between target object and surface of host material "D_0" is unknown. This makes also a paradox for estimating velocity through known depth, because depth of the rebar is the purpose of the survey. This issue is further solved by combining several algorithms of velocity measurement [15].

(e) Combination of algorithms—trilaterated ray path with object size and estimated object depth [15]

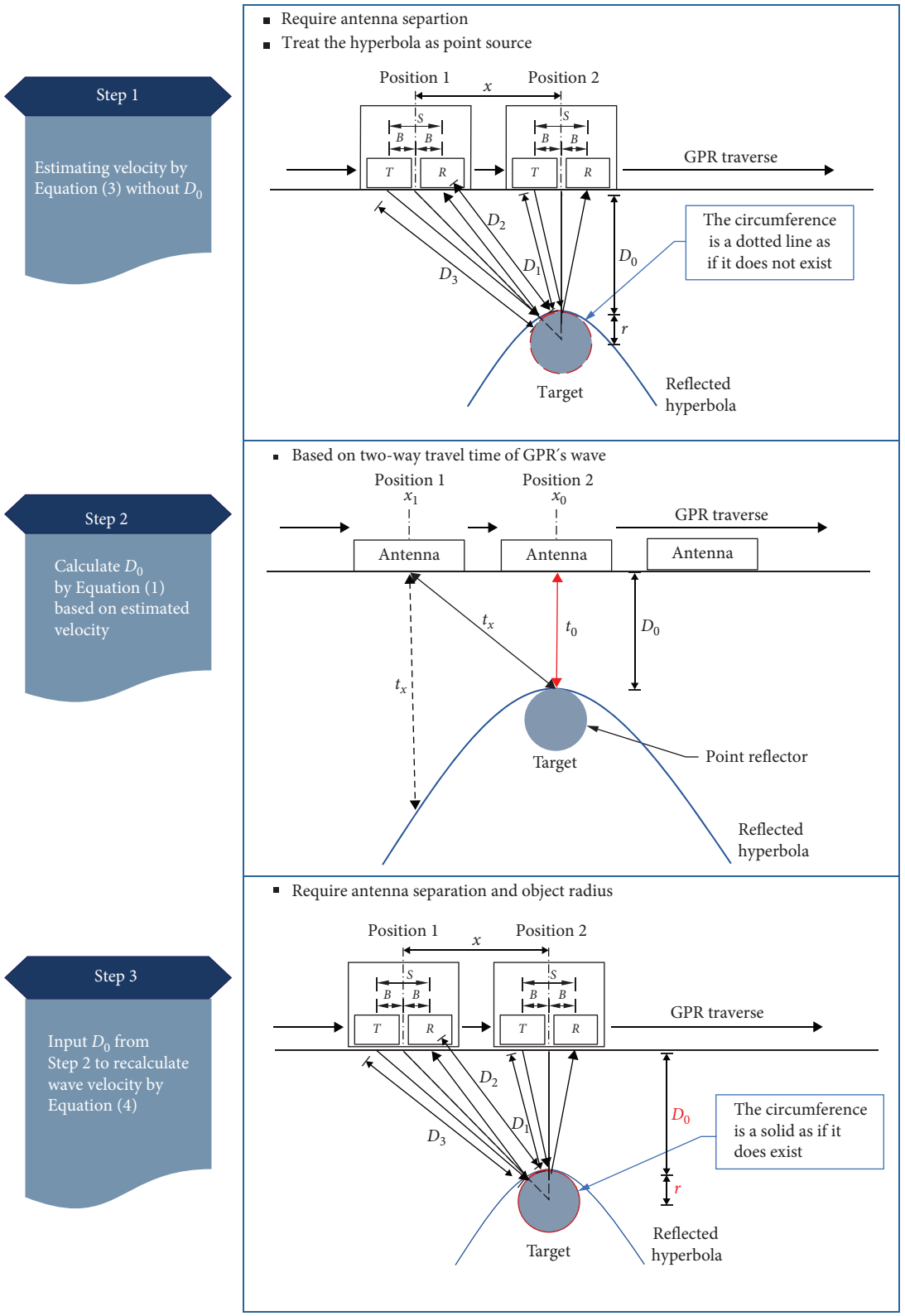

Figure 7: Workflow of the combined GPR wave velocity analytical method based on the geometry in Figure 6 [15].

This method considered the combination of algorithms to solve the problem in Equation (4), as shown in Figure 7. First, approximated GPR wave velocity "v" with consideration of antenna separation and target object as point source can be obtained by Equation (3). Second, based on approximated velocity "v," an "approximated" "D_0" is obtained by applying Equation (1). Finally, by inputting "approximated" "D_0," estimated "v" and "d" can be found in Equation (4) and

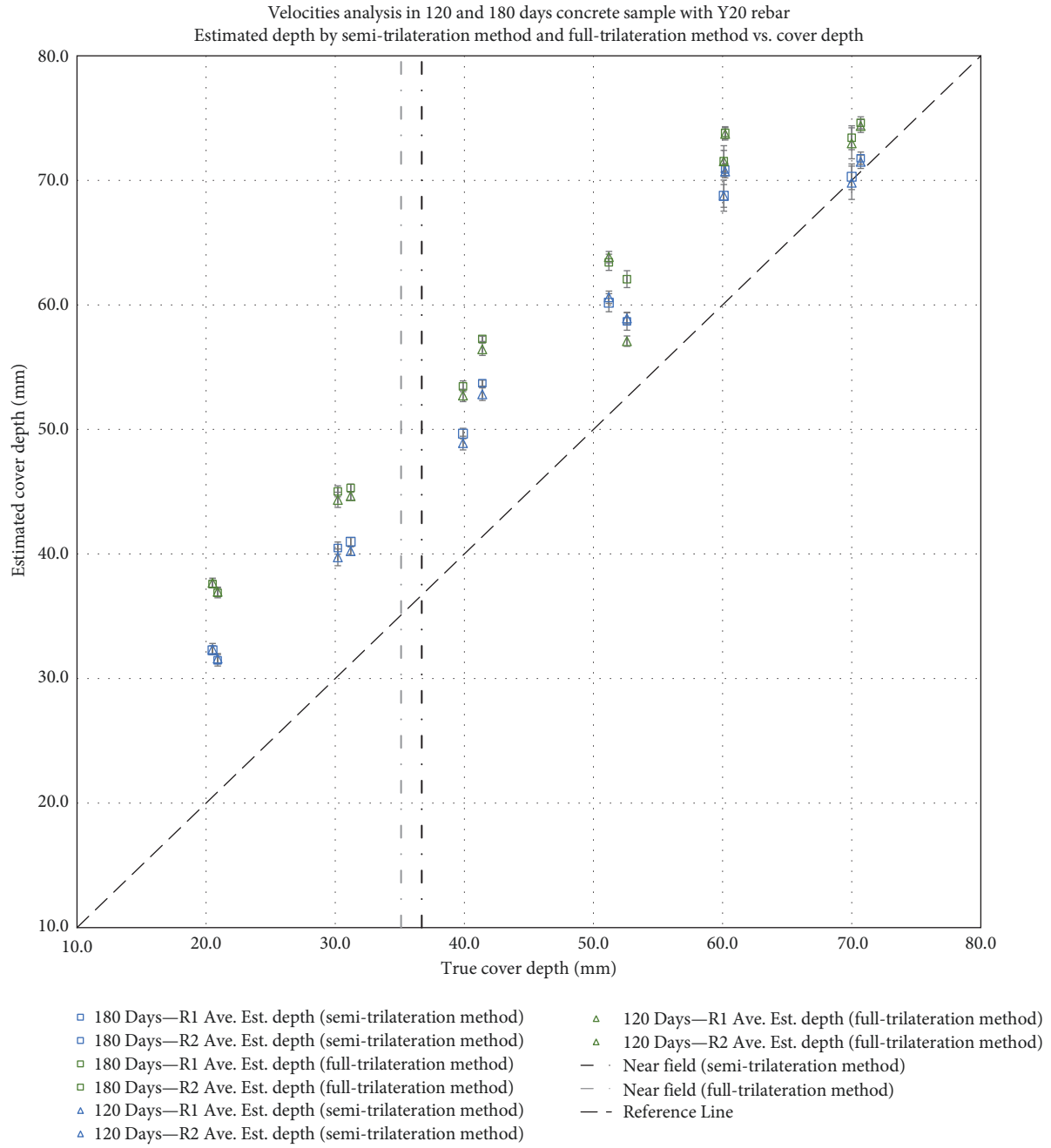

Figure 8: Estimated cover depths and actual cover depth by using semi-trilateration (Equation (3)) and full-trilateration (Equations (1), (3), and (4)) velocity analytical method.

Equation (1), respectively, where estimated "d" is the measurement of rebar cover depth. The advantages of this method are that the velocity outlier calculated by setting a standard deviation limit to 0.01 m/ns can be filtered, and velocity data points larger than 0.2998 m/ns (speed of light) can be computed along the data points at the diffractive hyperbolas. As shown in Figure 5, the proposed combination of velocity measurement method is a new approach for estimating GPR wave velocity by substituting mean of $v(x_i)$ in Equation (3) into V in Equation (1) to estimate D_0 then substitute the estimated D_0 in Equation (4) to recalculate $v(x_i)$ and D_0. Not also in this paper, the effect of included angle ($\sin\theta$) does not affect velocity estimation in Equations (3) and (4) because the GPR traverse is always perpendicular to the alignment of the buried linear object, which makes sin 90° is always equal to 1.

4. Findings and Discussion

4.1. Velocity Validation in Air. In homogeneous medium in air, GPR wave travels at a speed of light of 0.2998 m/ns. The estimated velocity from semi-trilateration equation, i.e.,

Equation (3), and full-trilateration equation, i.e., combined Equations (1), (3), and (4), with known object depth, can be compared with GPR wave in air. The experimental test using rebar in air can verify the constituency of the velocity analytical methods. The calculated discrete velocity using semi-trilateration equation and full-trilateration equation are highly consistent with 12 repetitive measurements, in which the semi-trilateration equation underestimates the GPR wave velocity slightly by 1.06% compared to the speed of light, while the result from the full-trilateration algorithm yields only 0.17% more than the speed of light due to measurement error. In view of the standard deviation of the measured velocity data, the velocity algorithm using semi- and full-trilateration algorithms are 0.0018 and 0.0016 m/ns, respectively. The result showed that the estimated GPR wave velocity in air by the models is highly accurate. This error is considered very small, and the result is thus satisfactory for the methodology to be used in concrete specimens.

4.2. Findings and Discussion in Control Concrete Experiments. Prior to conduct velocity analysis, all collected data were post-processed by standard data processing according to LSGI [19]. Velocity analysis was performed by semi-trilateration equation [14] and combined equation/full-trilateration equation [15], which was programmed in the in-house LabVIEW programme, as shown in Figure 5 [14]. The 2D velocity profiles were generated after applying a moving average filter.

The effects to accurately measure the depth of an object by a near-field GPR are crucial. According to the estimated cover depths result for a cover depth of 10–30 mm, as shown in Figure 8, the semi-trilateration and the full trilateration models overestimated the actual cover by 12.2–9.7 mm (136.1%–34.5%) and 17.5–14.1 mm (153.6%–46.1%), respectively. This overestimation was improved for a cover depth of 40–80 mm. The semi-trilateration and full-trilateration models overestimated the actual cover by 10.6–0.5 mm (28.2%–1.2%) and 14.3–3.5 mm (35.2%–5.0%), respectively. It reveals that the reactive near-field boundary for GSSI 2-GHz palm GPR antennae is approximately 40 mm. Based on the equation of $r = 0.62\sqrt{D^3/\lambda}$, where D is the aperture's maximum dimension which is 58.5 mm for the GPR used in this work and λ could range from 47.5 to 75.1 mm according to the wavelet transform, the calculated near-field reactive boundaries (r) are 36.6 and 35.0 mm by semi-trilateration and full-trilateration models respectively. Comparing the results, both results are matched to the obtained experimental result. This analysis justifies the trend of more accurate results can only be obtained along with a larger cover depth of the rebar, as shown in Figure 8. It also implies that the measurement of the cover depth of rebar is only reliable when the object locates in the Fresnel region. The results demonstrate an often neglected near-field phenomenon when GPR is called a reliable tool to measure the depth of buried objects. The results conveyed in this paper can also be extended to the mapping of deeper buried objects using lower GPR frequency by changing the parameters "D" and "λ." In other words, GPR users should bear in mind that the estimated depth is more reliable when the objects locate at the Fresnel region and becomes unreliable if the objects locate at the reactive near-field zone.

5. Conclusion

GPR practitioners always question the accuracy of GPR survey, and depth ranging is one of these questions. This paper provides solutions and recommendations in three aspects of understanding. First, this paper demonstrates a standard measurement method for cover depth estimation of buried objects by using semi- and full-trilaterated algorithms applied on the GPR diffractive hyperbolas, a much more accurate method than traditional hyperbolic fitting in commercial software. The advantage is that, on the one hand, the actual trilaterated ray path due to antenna separation and object alignment is considered. On the other hand, the depth of the object can be found by combined algorithms in lossless materials. Second, this paper explains the effects of reactive near-field and Fresnel region on the accuracy of depth measurement. It also demonstrates the measuring limits of the high-frequency 2-GHz antenna in shallow cover depth, i.e., <40 mm falling within the reactive near field. So, only depth beyond 40 mm is considered reliable because of the smaller deviation from the actual depth explained by the far-field theory. Third, it supplements the understanding of depth measurement errors with the often neglected and very simple linear model (Equation (2)) used by most commercial GPR processing software. It also follows that the developed methods can also be used to map other deeper objects with lower GPR frequency. Finally, our further works will be building an empirical correction model for depth measurement with more available data.

Data Availability

All data generated or analysed during this study are included in this published article.

Conflicts of Interest

The authors declare that they have no conflicts of interest.

Acknowledgments

Funding support by Hong Kong Research Grant Council (RGC)'s to the two RGC projects "Uncertainties Modelling on Depth Measurements of Buried Circular Objects in Ground Penetrating Radar Survey (PolyU/15218723)", "Multi-scale and Multi-array Ground Penetrating Radar (GPR) Diagnosis of Underground Hazards (PolyU/15216221)" and an Innovation and Technology Fund - Logistics and Supply Chain Multi-Tech R&D Centre (ITF-LSCM) project "Next-generation Imaging Technologies of Rapid Leakage Diagnosis of Underground High-Pressure and Large Water Mains in Carriageway (ITP/035/22LP)" are gratefully acknowledged.

References

[1] H. M. Jol, *Ground Penetrating Radar: Theory and Applications*, Elsevier B. V, 2009.

[2] P. Bienkowski and H. Trzaska, *Electromagnetic Measurements in the Near Field*, SciTech Publishing, Inc, 2012.

[3] J. D. Daniels, *Ground Penetrating Radar*, The Institution of Electrical Engineers, 2004.

[4] W. W. L. Lai, R. K. W. Chang, J. F. C. Sham, and K. Pang, "Perturbation mapping of water leak in buried water pipes via laboratory validation experiments with high-frequency ground penetrating radar (GPR)," *Tunnelling and Underground Space Technology*, vol. 52, pp. 157–167, 2016.

[5] W. W.-L. Lai, T. Kind, J. F.-C. Sham, and H. Wiggenhauser, "Correction of GPR wave velocity at different oblique angles between traverses and alignment of line objects in a common offset antenna settings," *NDT & E International*, vol. 82, pp. 36–43, 2016b.

[6] P. Wiwatrojanagul, R. Sahamitmongkol, S. Tangtermsirikul, and N. Khamsemanan, "A new method to determine locations of rebars and estimate cover thickness of RC structures using GPR data," *Construction and Building Materials*, vol. 140, pp. 257–273, 2017.

[7] N. Yazdani, E. Beneberu, and M. Riad, "Nondestructive evaluation of FRP-concrete interface bond due to surface defects," *Advances in Civil Engineering, Hindawi*, vol. 2019, Article ID 2563079, 10 pages, 2019.

[8] Z. Li and J. Desai, "Investigative assessment of concrete slab using non-destructive evaluation techniques," in *Structures Congress 2019: Buildings and Natural Disasters*, ASCE, 2019.

[9] F. Tosti and C. Ferrante, "Using ground penetrating radar methods to investigate reinforced concrete structures," *Surveys in Geophysics*, vol. 41, no. 3, pp. 485–530, 2020.

[10] T. Klewe, C. Strangfeld, and S. Kruschwitz, "Review of moisture measurements in civil engineering with ground penetrating radar—applied methods and signal features," *Construction and Building Materials*, vol. 278, no. 2021, Article ID 122250, 2021.

[11] E. C. Oikonomopoulou, V. A. Palieraki, I. P. Sfikas, and C. G. Trezos, "Reliability and limitations of GPR for identifying objects embedded in concrete—experience from the lab," *Case Studies in Construction Materials*, vol. 16, Article ID e00898, 2022.

[12] S. Tiwari and A. Soni, "Structure health monitoring of housing project: a case study," *Materials Today: Proceedings*, vol. 47, pp. 3783–3786, 2021.

[13] Y. Yang, J. Lu, R. Li, W. Zhao, and D. Yan, "Small-scale void-size determination in reinforced concrete using GPR," *Advances in Civil Engineering, Hindawi*, vol. 2020, Article ID 2740309, 11 pages, 2020.

[14] J. F. C. Sham and W. W. L. Lai, "Development of a new algorithm for accurate estimation of GPR's wave propagation velocity by common-offset survey method," *NDT & E International*, vol. 83, pp. 104–113, 2016.

[15] P. K.-W. Lau, B. W.-Y. Cheung, W. W.-L. Lai, and J. F.-C. Sham, "Characterizing pipe leakage with a combination of GPR wave velocity algorithms," *Tunnelling and Underground Space Technology*, vol. 109, Article ID 103740, 2021.

[16] W. L. Lai, T. Kind, and H. Wiggenhauser, "A study of concrete hydration and dielectric relaxation mechanism using Ground Penetrating Radar and Short-Time Fourier Transform," *EURASIP Journal on Advances in Signal Processing, Hindawi*, vol. 2010, Article ID 317216, 14 pages, 2010.

[17] ASTM Standard D6432, *Standard Guide for Using the Surface Ground Penetrating Radar Method for Subsurface Investigation*, ASTM International, West Conshohocken, PA, 2020.

[18] F. Xie, C. G.-W. Wu, W W.-L. Lai, and J. F.-C. Sham, "Correction of multi-frequency GPR wave velocity with distorted hyperbolic reflections from GPR surveys of underground utilities," *Tunnelling and Underground Space Technology incorporating Trenchless Technology Research*, vol. 76, pp. 76–91, 2018.

[19] Department of Land Surveying and Geo-informatics (LSGI), *Specifications for Non-destructive Testing, Surveying, Imaging and Diagnosis for Underground Utilities (NDTSID-UU) 1,2 Ground Penetrating Radar*, The Hong Kong Polytechnic University, 1st edition, 2019.